# Journal of Materials Chemistry C



## **PAPER**



Cite this: J. Mater. Chem. C, 2019, 7, 14949

## A novel reversible fluorescent probe for the highly sensitive detection of nitro and peroxide organic explosives using electrospun BaWO<sub>4</sub> nanofibers†

Gibin George, Da Caressia S. Edwards, Da Jacob I. Hayes, Lei Yu, b Sivasankara Rao Ede, Jianguo Wen b and Zhiping Luo \*\*

Fabrication of highly stable, reversible, and efficient portable sensors for the detection of explosives for safety and security is challenging due to the robustness of the currently available detection tools, limiting their mass deployment to the explosion prone areas. This paper reports a new direction towards the sensing of nitro- and peroxide-based explosives using highly stable rare-earth-doped BaWO<sub>4</sub> nanofibers with remarkable sensitivity and reversibility. BaWO<sub>4</sub> nanofibers doped with Tb<sup>3+</sup> and Eu<sup>3+</sup> ions are fabricated through a sol-gel electrospinning process, and their emission characteristics and application as a fluorescent probe for the sensing of 2-nitrotoluene and H<sub>2</sub>O<sub>2</sub>, explosive taggants representing a broad class of explosives, are studied in detail. Scheelite structured BaWO<sub>4</sub> nanofibers exhibit excellent luminescence characteristics, and the rare-earth ion doping in the polycrystalline BaWO<sub>4</sub> nanofibers is tailored to achieve blue, green, red, and white light emissions. These nanofibers are extremely sensitive to 2-nitrotoluene and  $H_2O_2$  with rapid response time, and sensitivity is observed within the range of 1-400 ppb and 1-10 ppm, towards 2-nitrotoluene and H<sub>2</sub>O<sub>2</sub>, respectively. The fluorescence quenching of BaWO<sub>4</sub> nanofibers in the presence of 2-nitrotoluene and H<sub>2</sub>O<sub>2</sub> is exponential with the quenching constants up to  $1.73 \times 10^6$  and  $2.73 \times 10^4$  L mol $^{-1}$ , respectively, which are significantly higher than those of most of the fluorescent probes based on metal-organic frameworks and conjugated organic materials. After exposing to 2-nitrotoluene, the luminescence of the nanofibers is retained completely upon heating at 120 °C for 10 min and the sensory response is retained as fresh nanofibers, and currently available fluorescent explosive sensors could not achieve such a recovery. The high sensitivity and selectivity of scalable rare-earth-doped BaWO<sub>4</sub> nanofibers provide a new platform for the simultaneous detection of two classes of explosives.

Received 13th September 2019, Accepted 30th October 2019

DOI: 10.1039/c9tc05068j

rsc li/materials-c

### Introduction

In recent years, for the sake of safety and security, the interest in the detection and quantification of nitro-organic compounds and organic peroxides, primary classes of explosives, is increased tremendously across the world. The current analytical techniques such as liquid chromatography-mass spectrometry (LC-MS), gas chromatography-mass spectrometry (GC-MS), high-performance liquid chromatography (HPLC), ion mobility spectrometry, proton transfer reaction mass spectrometry (PTR-MS), electrochemical methods, surface plasmon resonance (SPR), surface-enhanced

An explosive sensor requires exceptionally high sensitivity and low limit of detection (LOD) because of the very low vapor pressures of these compounds. Additionally, high selectivity is necessary to avoid false signals and should be available for mass deployment to cover the breadth of terrorist threats involving explosives.5 The major classes of explosives are organic nitrocompounds and organic peroxides. Due to the very low vapor pressures of these molecules, they are more likely to attach on surfaces with high surface energy such as metals, metal oxides, etc. as compared with low surface energy materials such as polymers, plastics, etc.5 Moreover, the higher surface-to-volume

Raman scattering (SERS), etc. for the detection of explosives require specialized training and miniaturization of such techniques is nearly infeasible. Therefore, fluorescence-based explosive sensors have been extensively studied for miniaturized portable devices,<sup>2</sup> especially, fluorescent nanostructured materials such as quantum dots<sup>3</sup> and metal-organic frameworks.<sup>4</sup> Developing a sensitive and selective sensor for the explosives, which is inexpensive and portable, is always of practical significance.

<sup>&</sup>lt;sup>a</sup> Department of Chemistry, Physics and Material Science,

Fayetteville State University, Fayetteville, NC 28301, USA. E-mail: zluo@uncfsu.edu

<sup>&</sup>lt;sup>b</sup> Centre for Nanoscale Materials, Argonne National Laboratory, Argonne, IL 60439, USA

<sup>†</sup> Electronic supplementary information (ESI) available: TGA results of precursor fibers, Rietveld refined XRD patterns, FTIR spectra and CIE diagram of BaWO<sub>4</sub> nanofibers, UV-visible spectra, schematic of the sensing mechanism and testing procedure, and photobleaching curves of nanofibers. See DOI: 10.1039/c9tc05068j

ratio of the nanomaterials enhances the interaction between the analyte and the sensor material.  $^6$ 

Photoluminescence-based sensors have been widely reported for the detection and quantification of explosive traces.<sup>7</sup> The performances of these sensors are based on the characteristics of the sensory materials used, for instance, the ability of the sensor materials to form a complex with the explosive molecules for photo-induced electron transfer (PET).<sup>8</sup> Besides, the overlapping of the emission spectrum of the sensory materials with the absorption spectrum of explosives is important in resonance energy transfer (RET)9 and protonation of fluorophores by analytes is necessary for intramolecular charge transfer (ICT).<sup>10</sup> The current organic fluorescent materials may be sensitive and efficient in determining nitro explosives; while their instability for repeated use is a significant concern. 11 The recovery of the luminescence of the hybrid organic sensor materials can be achieved only by subsequent washing, and most of the time, the sensitivity cannot be completely recovered, as observed in the case of luminescent metal-organic frameworks (MOFs). 12 The shortcomings such as stability, color tunability, broad emission, etc. of luminescent sensors can be overcome using rare-earth (RE<sup>3+</sup>) doped inorganic oxides and fluorides with sharp and tunable luminescence emission. The application of inorganic materials with high thermal and chemical stability and sharp emission is highly promising as fluorescent probes towards various chemicals. The recovery of the luminescence by these sensors is often possible by simply heating above the evaporation temperature of the explosive materials.

Scheelite structured materials are widely reported for their photophysical and photocatalytic activities. 13 Their photoluminescence sensing behavior is reported towards the sensitivity of H<sub>2</sub>O<sub>2</sub><sup>6</sup> and glucose. 14 Scheelites with the general formula AWO<sub>4</sub> (A = Ba, Sr, Ca, and Pb) are broadly studied for their luminescence, photocatalysis, and scintillation properties. 15 Among them, BaWO<sub>4</sub> is an important material, which is highly suitable for optical applications. For instance, BaWO4 crystals are identified as an efficient Raman-active material for utilization in picosecond solidstate laser systems, due to their high Stokes conversion efficiency in stimulated Raman scattering. 16 Eu3+-doped BaWO4 nanowires can improve the efficiency of dye-sensitized solar cells, resulting in an increase in efficiency by 15% as compared to the cell without BaWO<sub>4</sub>:Eu<sup>3+</sup> nanowires.<sup>17</sup> BaWO<sub>4</sub> is reported for a large number of other optical applications, such as in fluorescent sensors, 17 phosphors, light-emitting diodes, optical filters, scintillators, photocatalysis, and solid-state lasers. 18 The fabrication of BaWO4 nanostructures with different morphologies and sizes has been reported in the literature, such as whiskers, nanowires, penniform nanostructures, nanosheets and nanobelts, hollow spheres, dumbbells, and ellipsoids. 19 Nevertheless, electrospun BaWO<sub>4</sub> nanostructures with very high aspect ratios and their properties are nowhere reported in the literature.

One-dimensional nanoscale architectures are successfully integrated into nanoscale devices based on the optical, magnetic, and electronic properties of the materials.<sup>17</sup> Electrospinning is a widely accepted technique for the scalable fabrication of organic and inorganic nanofibers for many applications. The high aspect

ratio nanofibers have enhanced performances in terms of charge and energy transport compared to bulk materials or two-dimensional systems. Thus, luminescent organic/inorganic nanofibers are promising for the development of nanoscale light-emitting devices with high efficiency. Electrospun nanofibers are potential candidates for highly sensitive optical biosensors, an nanoscale optical waveguides, benefit filters, and novel laser architectures. Besides, electrospinning has a high throughput, is versatile, is cost-effective, and easily controls the shape and size of one-dimensional nanoscale architectures as compared to many conventional techniques.

In this work, we report the fabrication of ultra-long BaWO<sub>4</sub> nanofibers through a sol-gel electrospinning process and their sensitivity toward the detection of explosive taggants. The PL emission bands of the BaWO<sub>4</sub> nanofibers are tailored by Tb<sup>3+</sup> and Eu<sup>3+</sup> doping and the RE<sup>3+</sup> loading is optimized for white light emission. The cathodoluminescence (CL) emission of these nanofibers under high-energy electron beam irradiation is also studied for the potential application in high-energy radiation detection. RE<sup>3+</sup> doped nanofibers are highly sensitive to 2-nitrotoluene with a LOD of 35-45 nM, which is lower than that of MOF based sensors 12b,26 and comparable to that of CdSe quantum dots.<sup>27</sup> The fluorescence quenching of the nanofibers in the presence of analytes is reversible, and the nanofibers are successfully reused for the detection of explosives after subsequent heating, and such a recovery is not observed in the case of fluorescent probes for explosives reported in the literature. BaWO<sub>4</sub> luminescent nanofibers offer a highly stable and promising miniaturized alternative to conventional analytical techniques and organic materials for precise and sensitive detection of explosives.

## Materials and methods

#### Materials

Polyvinylpyrrolidone (PVP, MW:  $1.0 \times 10^6$ ), barium(II) acetate (Ba(Ac)<sub>2</sub>), ammonium metatungstate (AMT, assay 98%), and *N*,*N*-dimethylformamide (DMF) purchased from Sigma Aldrich were used without further purification to fabricate the precursor composite fibers. Europium acetate hydrate procured from Sigma Aldrich and terbium acetate hydrate from Alfa Aesar were used for RE<sup>3+</sup> doping. H<sub>2</sub>O<sub>2</sub> (50 W%) obtained from Acros organics and 2-nitrotoluene from Merck were used as the model explosives for sensing.

#### Electrospinning of BaWO<sub>4</sub> nanofibers

To prepare electrospinnable sol of PVP and the metal salts, the predetermined amounts of the acetate salts were dissolved in 20/80 water/DMF mixed solvent. To the above solution, ten w/v% of PVP was added and stirred magnetically for 10 min. Finally, the stoichiometric quantity of AMT was added and stirred overnight before it was loaded to the electrospinning unit (MSK-NFES-4, MTI Corporation). The electrospinning was carried out at an applied voltage of 18 kV, a tip to collector distance of 17 cm,

and a solution flow rate of 500  $\mu$ L h<sup>-1</sup>. The precursor composite fibers were collected on a rotating drum collector covered with an aluminum foil. The selection of the calcination temperature was based on the degradation temperature of the precursor composite fibers during their thermogravimetric analysis (TGA, Shimadzu DTG-60) in a nitrogen atmosphere at a heating rate of 10 °C min<sup>-1</sup>. The electrospun PVP/Ba(Ac)<sub>2</sub>/AMT composite nanofibers were then calcined at 700 °C, at a heating rate of 2 °C min<sup>-1</sup> with a dwell time of 5 h to obtain BaWO<sub>4</sub> nanofibers. The doped nanofibers were made using a similar method, in which respective molar percentages of acetate salts of the dopants are added to replace the subsequent amount of Ba(Ac)2, and the procedure above was followed. All the doped BaWO<sub>4</sub> nanofibers were calcined at 700 °C. The doped nanofibers are represented as BaWO<sub>4</sub>:xTb-yEu, where x and y are the respective mol% of RE<sup>3+</sup> ions.

#### Characterization of BaWO<sub>4</sub> nanofibers

The morphology of the BaWO<sub>4</sub> nanowires was identified using a JEOL field-emission JXA-8530F electron probe microanalyzer (EPMA), after coating the samples with an  $\sim 5$  nm carbon film (Denton carbon coater). An EPMA was equipped with an X-ray energy dispersive spectrometer (EDS) for chemical compositional analysis, and an xCLent IV Advanced B Hyperspectral Cathodoluminescence (CL) detector for the CL analysis. The nanofibers for transmission electron microscopy (TEM) were prepared in pure ethanol solutions, sonicated for 1 min and then dispersed on carbon-film supported grids. The grids were observed in an FEI Talos F200X TEM/STEM instrument at 200 kV. The scanning TEM (STEM) imaging was done in the STEM mode using a high-angle annular dark-field (HAADF) imaging detector, and the elemental maps of selected elements were collected using the X-ray EDS signals. The X-ray diffraction (XRD) patterns of the nanofibers were recorded using a Rigaku MiniFlex 600 X-ray diffractometer in the scan range of 10-90° and a scan speed of 0.06 deg min<sup>-1</sup>. Fourier-transform infrared (FTIR) spectra (IRPrestige-21, Shimadzu) were recorded in the transmission mode by the KBr pellet method in the wavenumber range of 300-4000 cm<sup>-1</sup> at an average of 32 scans. The photoluminescence spectra of the samples were obtained in powder form recorded using a Shimadzu RF-5301PC spectrofluorophotometer at room temperature, and the sensitivity measurements were also performed using the same instrument. The UV-visible spectra were recorded using Cary 100 Bio UV-visible spectrophotometer.

#### Sensitivity measurements

To test the sensitivity towards the explosives, 2-nitrotoluene and H<sub>2</sub>O<sub>2</sub> were used as the detection taggants. 5 mg of the BaWO<sub>4</sub> nanofiber phosphor was dispersed in 50 mL of deionized water, and the concentrations of 2-nitrotoluene and H2O2 were subsequently adjusted in the solution, and the PL emission spectra were recorded for different concentrations of taggants. To test the selectivity, the PL emissions from the nanowires in the presence of Cu(NO<sub>3</sub>)<sub>2</sub> (Cu<sup>2+</sup>), Fe(NO<sub>3</sub>)<sub>3</sub> (Fe<sup>3+</sup>), glucose, AgNO<sub>3</sub> (Ag<sup>+</sup>), Ba(NO<sub>3</sub>)<sub>2</sub> (Ba<sup>2+</sup>), Pb(NO<sub>3</sub>)<sub>3</sub> (Pb<sup>2+</sup>), Cr(NO<sub>3</sub>)<sub>3</sub> (Cr<sup>3+</sup>), HCl (2 pH) and NaOH (14 pH)

were recorded. The selectivity towards other nitro-aromatic compounds is studied using 4-nitrotoluene and 3-nitrophenol as the representative analytes. To study the sensitivity of the nanofibers in the solid state, the nanofibers are pasted on a glass substrate using SCOTCH double-sided tape. The nanofibers are then exposed to 2-nitrotoluene vapors generated by heating appropriate quantities of 2-nitrotoluene in a Petri dish. The PL spectra of the nanofibers are then recorded. The 2-nitrotoluene vapors from the nanofibers were removed by heating at 120 °C for 10 minutes in a conventional oven and the PL spectra are recorded. The process is repeated up to 10 times to check the reversibility of the fibers in detecting the nitroaromatic compounds.

## Results and discussions

The TGA and DTA plots of PVP/Ba(Ac)2/AMT composite nanofibers are shown in Fig. S1 (ESI†). The precursor composite nanofibers exhibit three-steps in their thermal degradation process before they are completely transformed into BaWO<sub>4</sub> nanofibers, whereas the pure PVP exhibits a single step in its thermal degradation profile.<sup>28</sup> The actual onset of degradation of the composite nanofibers is at  $\sim 250$  °C and the degradation is completed at  $\sim$  475 °C. The removal of water from the nanofibers is evident in the first step of the degradation process at  $\sim 100$  °C. The conversion of the organic part of the salts commences during the second step of the degradation process at  $\sim 250$  °C. The complete elimination of the volatile part of the salts and PVP takes place in the final step. The DTA curve exhibits multiple exothermic and endothermic phase transformations during the degradation process. Though there is no remarkable weight loss above 475 °C, the exothermic reaction continues at high temperatures as evident from the DTA peaks above 500 °C, which essentially reveals the calcination temperature to be  $\sim 700$  °C.

#### Morphology and structure

The successful formation of pure and RE3+ doped BaWO4 nanofibers from the precursor composite nanofibers was confirmed with the XRD results shown in Fig. 1. The BaWO<sub>4</sub> nanofibers obtained after calcination are completely crystalline as indicated by the very sharp peaks in the XRD patterns of the nanofibers. The structure of BaWO<sub>4</sub> nanofibers can be indexed to the JCPDS standard data file No. 01-085-0588, with a space group of  $I4_1/a$ (No. 88) (a = 5.613 Å and c = 12.72 Å). XRD patterns of the RE<sup>3+</sup> doped BaWO<sub>4</sub> nanofibers reveal that the crystal structure of BaWO<sub>4</sub> remains unaffected by the dopants since there is no apparent peak of the dopant oxide in the XRD pattern of the respective nanofibers. Table 1 lists the lattice parameters and cell volume of BaWO4:RE3+ nanofibers obtained by Rietveld refinement of the XRD patterns, as shown in Fig. S2 (ESI†).

The RE<sup>3+</sup> ions replace the lattice site of Ba<sup>2+</sup> ions, and the size of RE<sup>3+</sup> ions is smaller than that of the Ba<sup>2+</sup> ions. Therefore, a change in the lattice parameter and the reduction in unit cell volume are expected, and the same is observed during the refinement. Fig. 2a and b shows the electrospun BaWO4 nanofibers

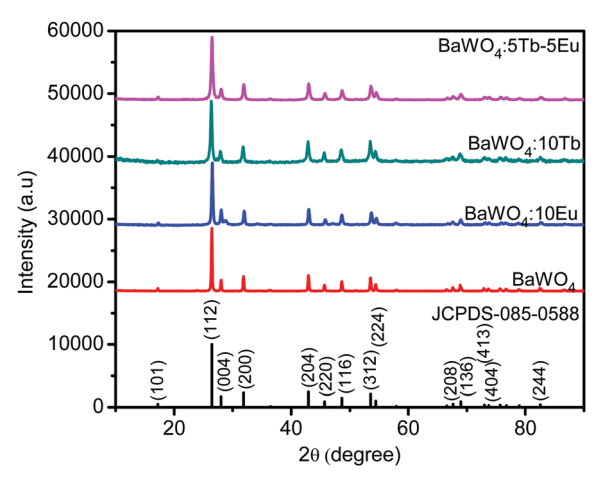


Fig. 1  $\,$  Comparison of XRD patterns of pure and doped BaWO\_4 nanofibers calcined at 700  $^{\circ}\text{C}.$ 

obtained after calcining at 700  $^{\circ}$ C. The SEM images reveal that the fibers are randomly oriented and continuous. The high magnification images reveal the porous nature of the fibers. In the EDS spectrum of the representative (Fig. 2c) nanofibers, the peaks corresponding to Ba, W and O, and the representative dopants are present.

The representative TEM images of the BaWO<sub>4</sub> nanofibers are shown in Fig. 3. The TEM images reveal that the nanofibers are 156 nm in average diameter with a standard deviation of 10.6 nm, based on 20 measurements, and are polycrystalline in nature, with a grain size of  $\sim 30$  nm (Fig. 3a, inset). The rings in the SAED pattern in Fig. 3b also reveal the polycrystalline nature of the nanofibers with high crystallinity. The nanosized grains comprising the fibers are randomly oriented, and they are formed due to homogeneous nucleation and the space confinement of the nanofibers. The measured *d*-spacings from the high-resolution TEM (HRTEM) image (Fig. 3c) are consistent with the XRD results. The TEM-EDS elemental maps of the BaWO<sub>4</sub>:5Tb–5Eu nanofibers shown in Fig. 4 reveal that the Tb³+ and Eu³+ ions are uniformly dispersed in the BaWO<sub>4</sub> nanofiber lattice.

The complete elimination of organic parts from the precursor composite fibers is confirmed with the FTIR spectra (Fig. S3, ESI†). In the spectra of PVP/Ba(Ac)<sub>2</sub>/AMT composite nanofibers, the broad peak at 3453 cm<sup>-1</sup> is due to the –OH stretching. The peaks at 2957 and 2882 cm<sup>-1</sup> represent the symmetric and asymmetric vibrations of CH in CH<sub>2</sub> and CH<sub>3</sub>, respectively. The peaks at 1648, 1411, and 1288 cm<sup>-1</sup> are attributed to C=O, CH<sub>2</sub> bending, and C=N vibrations, respectively. The broad peak

**Table 1** Lattice parameters and cell volume of BaWO₄:Re<sup>3+</sup> nanofibers

	Lattice parameter (Å)			
Sample	$\boldsymbol{A}$	C	Volume (cubic Å)	
BaWO4	5.6232	12.7437	402.96	
BaWO4:Tb	5.6108	12.7603	401.71	
BaWO4:5Eu	5.6114	12.7331	400.94	
BaWO4:5Tb-5Eu	5.6095	12.7257	400.43	

between 800 and 400 cm<sup>-1</sup> is due to the several vibrational modes of the pyrrolidone ring.<sup>31</sup> The pure and doped nanofibers of BaWO<sub>4</sub> exhibit a significant broad peak at ~835 cm<sup>-1</sup>. In BaWO<sub>4</sub>, the [WO<sub>4</sub>]<sup>2-</sup> ligand has  $T_{\rm d}$  point group symmetry. Therefore, the irreducible vibrational modes can be written as  $\Gamma_{T_{\rm d}} = A_1(\nu_1) + E(\nu_2) + F_2(\nu_3) + F_2(\nu_4)$ , in which  $F_2(\nu_3,\nu_4)$  modes are IR active. Hence, the peak at ~835 cm<sup>-1</sup> can be assigned to  $F_2(\nu_3)$  anti-symmetric stretching vibrations for BaWO<sub>4</sub>.<sup>32</sup>

#### **Photoluminescence**

The PL and photoluminescence excitation (PLE) spectra of pure BaWO<sub>4</sub> and doped BaWO<sub>4</sub> nanofibers are shown in Fig. 5. On comparing the PLE spectra of pure and RE<sup>3+</sup> doped nanofibers, one can observe the significant transition of the blue emission characteristic of [WO<sub>4</sub>]<sup>2-</sup> ligands to green and red corresponding to Tb<sup>3+</sup> and Eu<sup>3+</sup>, respectively. The PLE spectra of pure BaWO<sub>4</sub> nanofibers exhibit a broad absorption peaking at 247 nm, for the emission monitored at 440 nm, which is characteristic of the <sup>1</sup>A<sub>1</sub> ground state absorption of the [WO<sub>4</sub>]<sup>2-</sup> unit. The broad asymmetric blue-green PL spectra of BaWO<sub>4</sub> nanofibers constitute two peaks in the UV-blue region and blue-green region when excited by a 247 nm source, which originates by the charge transfer in the  $[WO_4]^{2-}$  complexes with the  $T_d$  symmetry groups or selftrapped electron states. 33 In the case of BaWO<sub>4</sub>:5Tb nanofibers, the PLE spectrum is monitored at 545 nm emissions, exhibiting several bands between 250 and 400 nm originating from the  $4f^8 \rightarrow 4f^75d^1$  transition of  $Tb^{3+}$  ions.<sup>34</sup> However, the broad absorption peak of the host matrix is also present in the PLE spectra. The sharp peaks observed at 488, 544, 590 and 620 nm originated from the  ${}^5\mathrm{D}_4 \to {}^7\mathrm{F}_6, {}^5\mathrm{D}_4 \to {}^7\mathrm{F}_5, {}^5\mathrm{D}_4 \to {}^7\mathrm{F}_4$  and  ${}^5\mathrm{D}_4 \to$ <sup>7</sup>F<sub>3</sub> 4f-4f transitions of Tb<sup>3+</sup> ions, respectively.<sup>35</sup> On comparing the PLE spectra of BaWO<sub>4</sub>:5Tb nanofibers with those of BaWO<sub>4</sub>:5Tb-5Eu nanofibers, several additional peaks appeared in the latter, due to the intra-configurational f-f transitions of Eu<sup>3+</sup>. In the respective PLE spectrum, in addition to the broad excitation peak of the BaWO<sub>4</sub> matrix at 247 nm, dominant peaks at 364, 377, 394, 410 and 464 nm are also observed, which correspond to  ${}^7F_0 \rightarrow {}^5D_4, {}^7F_0 \rightarrow {}^5D_2, {}^7F_0 \rightarrow {}^5L_6, {}^7F_0 \rightarrow {}^5D_3$  and  $^{7}F_{0} \rightarrow ^{5}D_{1}$ , respectively, of Eu<sup>3+</sup> ions. Overlap of the emission bands of BaWO<sub>4</sub> with the excitation bands of Tb<sup>3+</sup> and Eu<sup>3+</sup> reveals the apparent resonance type energy transfer between the matrix and the ions.<sup>36</sup> The red emission spectra of characteristic Eu<sup>3+</sup> ions from BaWO<sub>4</sub>:5Tb-5Eu signify the energy transfer between Tb3+ and Eu3+. The red Eu3+ emission can be ascribed to the intrinsic 4f-4f ( $^{7}D_{4}^{7} \rightarrow F_{0-7}$ ) transitions, and to be precise, the emission peaks at 578, 592, 612, 654, and 702 nm are assigned to  ${}^5D_4{}^7 \rightarrow F_0$ , 5  ${}^5D_4 \rightarrow {}^7F_1$ ,  ${}^5D_4 \rightarrow {}^7F_2$ ,  ${}^5D_4 \rightarrow {}^7F_3$ , and  ${}^5\mathrm{D}_4 \rightarrow {}^7\mathrm{F}_4$  transitions of Eu $^{3+}$ , respectively.  $^{37}$ 

PL spectra of BaWO<sub>4</sub>:xTb nanofibers are shown in Fig. 6a. The PL spectrum consists of strong characteristic peaks of Tb<sup>3+</sup> ions originating from 4f-4f transitions when excited by a 247 nm wavelength source. The emission characteristic of the BaWO<sub>4</sub> matrix completely disappeared on doping with Tb<sup>3+</sup>, and the significant sharp 4f-4f green emissions of Tb<sup>3+</sup> ions are evident at every concentration of Tb<sup>3+</sup> ions. Therefore, the nonradiative energy transfer from the matrix to Tb<sup>3+</sup> ions is evident

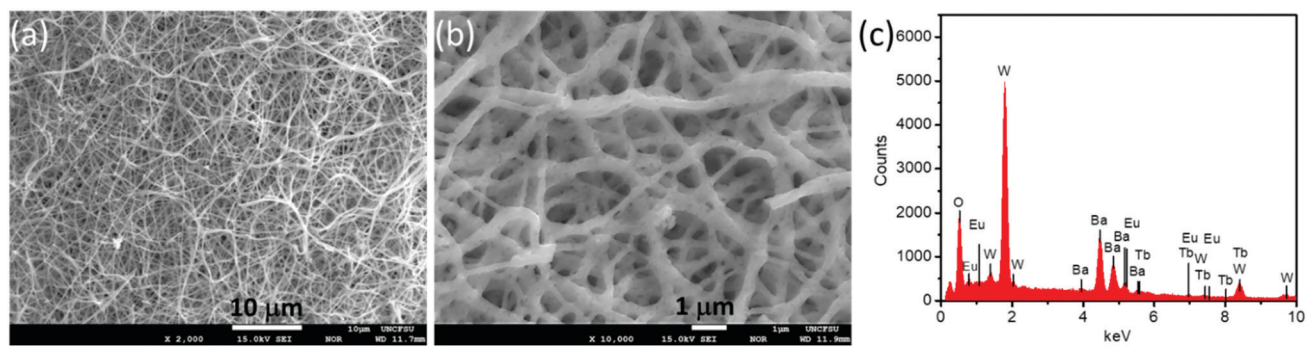


Fig. 2 (a) Low and (b) high magnification SEM images of representative BaWO<sub>4</sub> nanofibers; and (c) EDS spectrum of BaWO<sub>4</sub>:5Tb-5Eu nanofibers

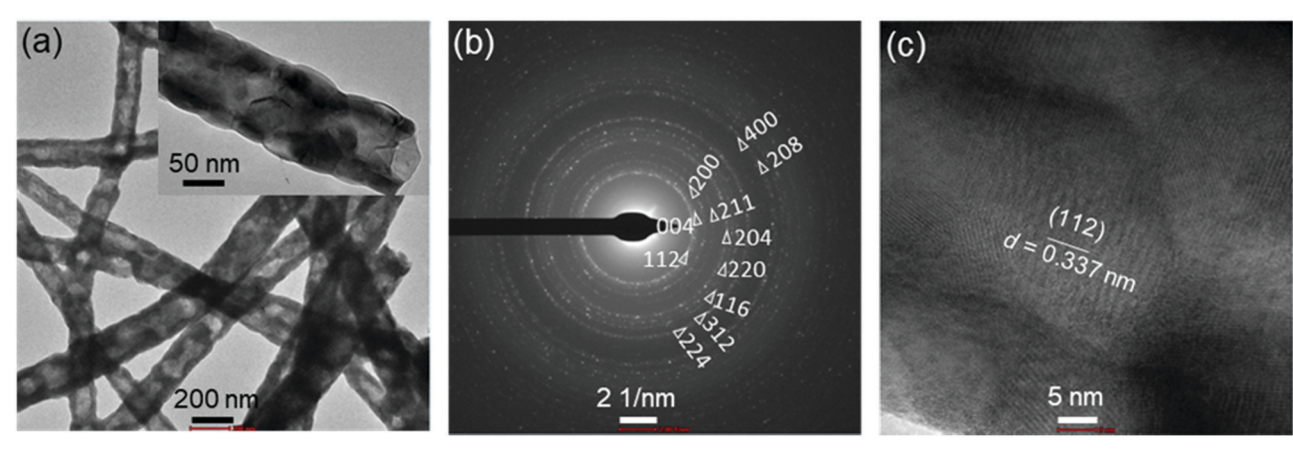


Fig. 3 (a) TEM, (b) SAED patterns, and (c) HRTEM images of BaWO<sub>4</sub>:5Tb-5Eu nanofibers.

in these nanofibers. The intensity of emission from Tb<sup>3+</sup> ions gradually decreased with Tb3+ concentration, and the most intense emission is observed from the nanofibers doped with 5 mol% of Tb<sup>3+</sup> ions. The reduction in Tb<sup>3+</sup> emission intensity at higher concentrations above 15 mol% could be attributed to Tb<sup>3+</sup>-Tb<sup>3+</sup> internal concentration quenching, during which the excitation energy is lost by the energy migration among the activator ions.

In the PL spectra of BaWO<sub>4</sub>:5Tb-zEu nanofibers, as shown in Fig. 6b, strong emissions in the orange-red region are observed. As the Eu<sup>3+</sup> concentration is increased, the red emission intensity increases monotonically; at the same time, the intensity of Tb3+ ions is drastically decreased. The emission from Tb<sup>3+</sup> ions completely disappeared when the Eu<sup>3+</sup> concentration is 5%. In both 1% and 3% Eu3+ doped BaWO4 nanofibers, the characteristic emissions from both Tb3+ and Eu3+ ions are dominant. In all the instances, the intensity of the Eu<sup>3+</sup> emission line at 616 nm is significant in comparison to the emission at 591 nm. The PL emission at 616 nm, an electric dipole transition of Eu<sup>3+</sup> ions, is very sensitive to the local environment and the symmetry of the crystal field. However, the emission at 593 nm is not influenced well by the crystal field, which is a magnetic dipole transition of Eu<sup>3+, 38</sup> Therefore, Eu<sup>3+</sup> ions are in an asymmetric environment without inversion symmetry, meaning, in the BaWO<sub>4</sub> host matrix, RE<sup>3+</sup> ions replace Ba<sup>2+</sup> ions with tetragonal symmetry (S4 point symmetry). Moreover, the electronic densities of RE<sup>3+</sup> and Ba<sup>2+</sup> and their coordination numbers are analogous, despite the lower symmetry due to the valence mismatch between RE3+ and Ba<sup>2+</sup> ions and the resulting charge compensating defects.<sup>39</sup>

The CIE diagrams and the corresponding coordinates of the nanofibers when excited by a 247 nm source are presented in Fig. S4 (ESI†) and Table 2, respectively. The emission from the nanowires is scattered in the blue, green, and red regions. White light is also produced in the case of nanofibers doped with Tb<sup>3+</sup> and Eu<sup>3+</sup>. Therefore, the color of the emission can be controlled precisely by adding the appropriate amount of the dopant.

#### Cathodoluminescence characteristics

The cathodoluminescence (CL) spectra of the pure and doped BaWO<sub>4</sub> nanofibers are recorded under 10 kV and 100 nA electron beam, aimed to simulate the response of the nanofibers towards high energy radiation. The characteristic CL emission spectra are shown in Fig. 7. The pure BaWO<sub>4</sub> nanofibers emit a broad visible spectrum in the wide range of 300-750 nm (majorly blue and green bands) when excited by an electron beam, which is similar to the PL emission characteristics. The CL emission in the pure lattice originated from the propagation of ionization initiated by the fast-primary electrons. The ultraviolet light and visible light usually excite the activator directly; the fast electrons as highenergy particles always excite the host lattice. 40 Similar to other isomorphous scheelite structures, the CL emission spectra of

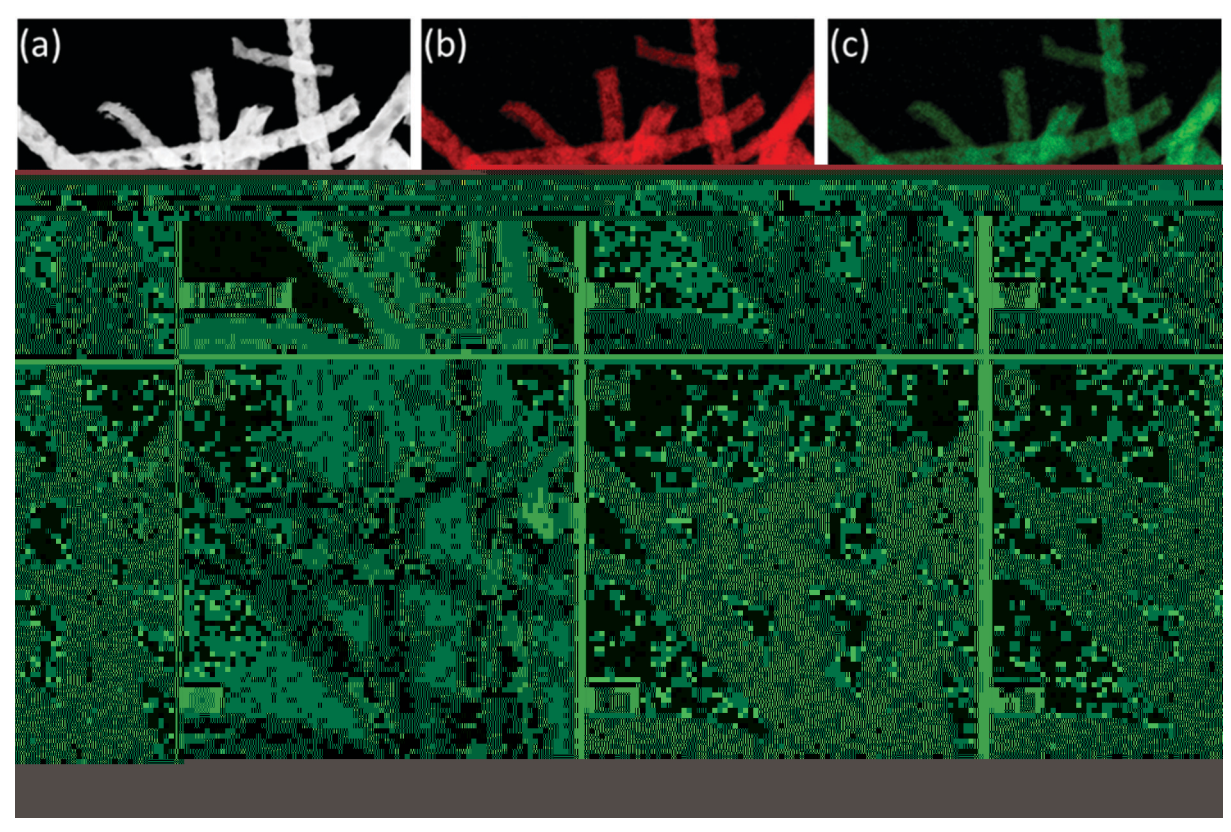


Fig. 4 (a) TEM-HAADF image and (b)-(f) show the corresponding elemental maps by EDS of BaWO<sub>4</sub>:5Tb-5Eu nanofibers.

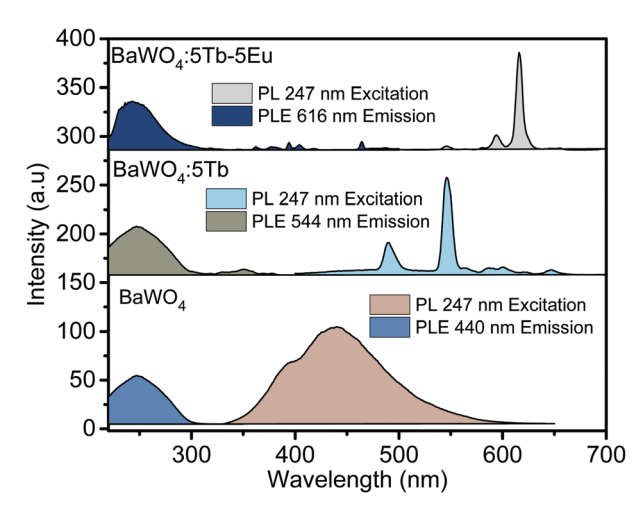


Fig. 5 PL and PLE spectra of pure  $BaWO_4$  and  $RE^{3+}$  doped  $BaWO_4$  nanofibers in the solid state.

BaWO<sub>4</sub> are akin to electronic transitions that take place within the [WO<sub>4</sub>]<sup>2-</sup> ions, which is evident in the PL spectrum of pure BaWO<sub>4</sub>. According to crystal field theory, for [WO<sub>4</sub>]<sup>2-</sup> ligands with  $T_{\rm d}$  symmetry, the ground state is  $^{1}{\rm A}_{1}$ , and there are four singlet excited states  $^{1}{\rm A}(^{1}{\rm T}_{1})$ ,  $^{1}{\rm E}(^{1}{\rm T}_{1})$ ,  $^{1}{\rm E}(^{1}{\rm T}_{2})$ , and  $^{1}{\rm B}(^{1}{\rm T}_{2})$ . The blue emission band is due to an intrinsic emission due to an electron transition  $^{1}{\rm B}(^{1}{\rm T}_{2}) \rightarrow {}^{1}{\rm A}_{1}$  of the [WO<sub>4</sub>]<sup>2-</sup> complex ions, and the green emission band is due to the WO<sub>3</sub> defects that are associated with oxygen vacancies.<sup>41</sup>

In the CL spectra of BaWO<sub>4</sub>:5Tb and BaWO<sub>4</sub>:5Tb-(1,5)Eu nanofibers, the emission peaks originating from the BaWO<sub>4</sub> lattices entirely disappeared. The CL spectra of BaWO<sub>4</sub>:5Tb nanofibers comprise the most intense emission lines at 544 nm, which is due to the Tb<sup>3+</sup> ions as in the PL spectra. Since the emission from the BaWO<sub>4</sub> lattices completely disappeared in the CL spectra, the energy transfer from the host lattice to Tb<sup>3+</sup> ions is recognized. All the possible transitions of Tb<sup>3+</sup> are visible in the CL spectra, which does not appear in the PL spectra. The several small peaks in the blue region < 450 nm are due to  ${}^5D_3 \rightarrow {}^7F_I(J=6,5,4,3)$  transitions and the peaks in the green region >450 nm are due to  ${}^5D_4 \rightarrow {}^7F_I$ (J=6, 5, 4, 3) transitions of Tb<sup>3+</sup> ions. 40 The emission band from Eu<sup>3+</sup> ions appeared in BaWO<sub>4</sub>:5Tb-(1,5)Eu nanofibers. The emission lines characteristic of Tb3+ ions are present in all the CL spectra of the doped nanofibers. The emission intensity from Eu<sup>3+</sup> ion doped BaWO<sub>4</sub>:5Tb-(1,5)Eu nanofibers is remarkable, which is dependent on the Eu<sup>3+</sup> concentration. The emission from Tb<sup>3+</sup>/Eu<sup>3+</sup> doped nanofibers is independent of the emission from the Tb<sup>3+</sup> ions. The simultaneous emission observed from Tb<sup>3+</sup> and Eu<sup>3+</sup> ions is possibly due to the contemporary energy transfer to these ions from the lattice. Therefore, in the case of doped nanofibers, the secondary electrons excite the host lattice and create many electron-hole pairs, leading to the formation of bound excitons. As no luminescence from bound exciton recombination is observed, these excitons, if formed, decay non-radiatively through a resonant or quasi-resonant transfer to the 4f shell of Eu<sup>3+</sup> and/or Tb<sup>3+</sup> ions and give their characteristic emission.42

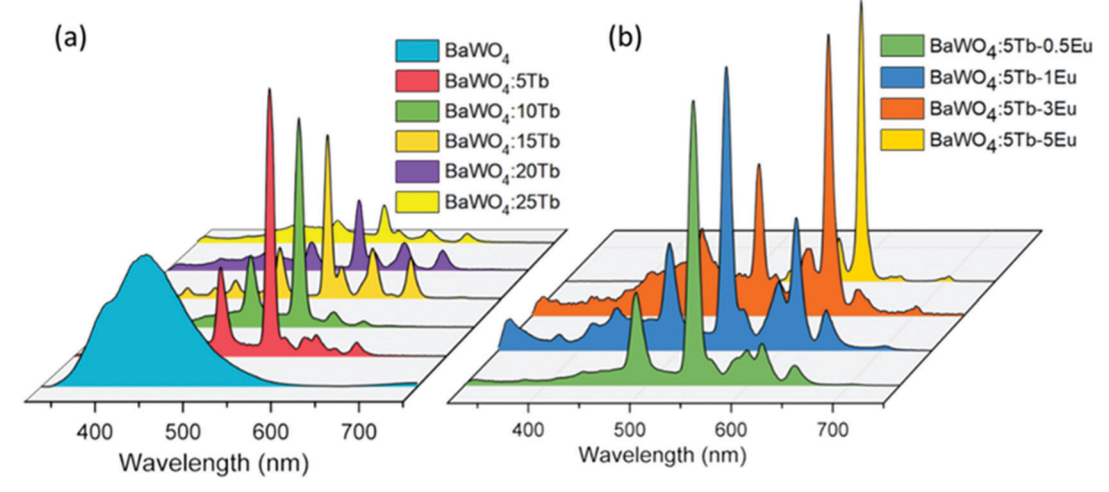


Fig. 6 PL spectra of (a) BaWO<sub>4</sub>:xTb and (b) BaWO<sub>4</sub>:5Tb-yEu nanofibers under 247 nm excitation in the solid state.

Table 2 CIE coordinates calculated from the PL spectra of BaWO<sub>4</sub> nanofiber phosphors

S. no.	Sample composition	CIE $(x)$	CIE (y)
1	BaWO <sub>4</sub>	0.1569	0.1257
2	BaWO₄:5Tb	0.2849	0.5118
3	BaWO <sub>4</sub> :10Tb	0.2479	0.5102
4	BaWO₄:15Tb	0.3498	0.4975
5	BaWO <sub>4</sub> :20Tb	0.3154	0.3615
6	BaWO <sub>4</sub> :25Tb	0.2507	0.3101
7	BaWO₄:5Tb−0.5Eu	0.3182	0.4976
8	BaWO₄:5Tb−1.0Eu	0.3478	0.4103
9	BaWO₄:5Tb−3.0Eu	0.3683	0.3556
10	BaWO <sub>4</sub> :5Tb-5.0Eu	0.6335	0.3498

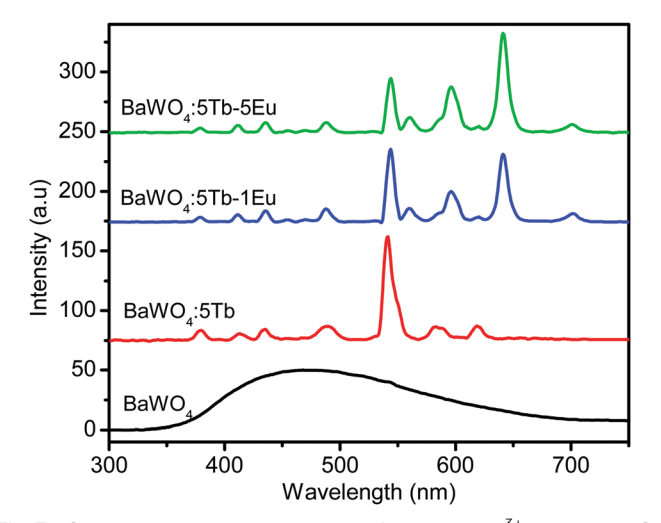


Fig. 7 Cathodoluminescence emission of pure and  $RE^{3+}$  doped  $BaWO_4$ nanofibers.

### Photoluminescence sensitivity towards 2-nitrotoluene and H<sub>2</sub>O<sub>2</sub>

The PL response of BaWO<sub>4</sub> nanofibers upon exposure to the model explosive taggants 2-nitrotoluene and H<sub>2</sub>O<sub>2</sub> is investigated by dispersing the nanofibers in water. The sensing performance of representative RE3+ doped BaWO4 nanofibers dispersed in water is tested by recording the fluorescence spectra in the presence of different concentrations of 2-nitrotoluene, as shown in Fig. 8a-c. The PL spectra of nanofiber dispersions in the presence of different concentrations of 2-nitrotoluene, ranging from 10 ppb to 400 ppb, clearly show a change in the fluorescence of RE3+ doped BaWO4 nanofibers concerning 2-nitrotoluene concentration. The quenching of the luminescence emission in the presence of 2-nitrotoluene in few parts per billion is rapid. The intensity of all RE<sup>3+</sup> emission bands is decreased simultaneously in the presence of 2-nitrotoluene, when excited by a 247 nm source. The presence of 2-nitrotoluene can be quantified for concentrations between 10 and 400 ppb. Additionally, the selectivity of the sensory materials was tested with glucose, Fe<sup>3+</sup>, Cu<sup>2+</sup>, Ba<sup>2+</sup>, Ag<sup>+</sup>, Pb<sup>2+</sup>, Cr<sup>2+</sup>, and pH, as shown in Fig. 8d and the corresponding PL spectra are shown in Fig. S5 (ESI†). The sensitivity towards other nitroaromatic compounds is confirmed using 4-nitrotoluene and 3-nitrophenol as the representative analytes. Their addition up to 1000 ppm to the BaWO4:5Tb-5Eu dispersion leads to insignificant modifications to the luminescence intensity, whereas the addition of 400 ppb of 2-nitrotoluene and 1000 ppb of  $H_2O_2$  leads to a >95% decrease. The excellent selectivity of the sensor nanofibers towards 2-nitrotoluene and H<sub>2</sub>O<sub>2</sub>, as compared to other disturbants, highlights RE<sup>3+</sup> doped BaWO<sub>4</sub> nanofibers as a promising fluorescent probe for the detection of explosives even at nM concentrations. The mechanism involved in the detection process can be related to the quenching of the RE<sup>3+</sup> emission.

In general, nitro compounds are electron-deficient, and quenching of fluorescence occurs via photoinduced donoracceptor electron transfer mechanism, <sup>2d</sup> where RE<sup>3+</sup> ions are donors and 2-nitrotoluene molecules are acceptors, which does not exhibit any luminescence. BaWO<sub>4</sub> crystallizes with  $[WO_4]^{2-}$ tetrahedrons on the surface covering the Ba<sup>2+</sup> ions, as a result, the surface of BaWO<sub>4</sub> exhibits a partial negative ( $\delta^-$ ) charge as in the case of CaWO<sub>4</sub> due to the high surface density of active oxygen atoms. 43,44 The crystal structure of BaWO4 is shown in Fig. S6 (ESI†). Importantly,  $[WO_4]^{2-}$  is the anion of strong tungstic acid with a susceptibility towards positive charges.

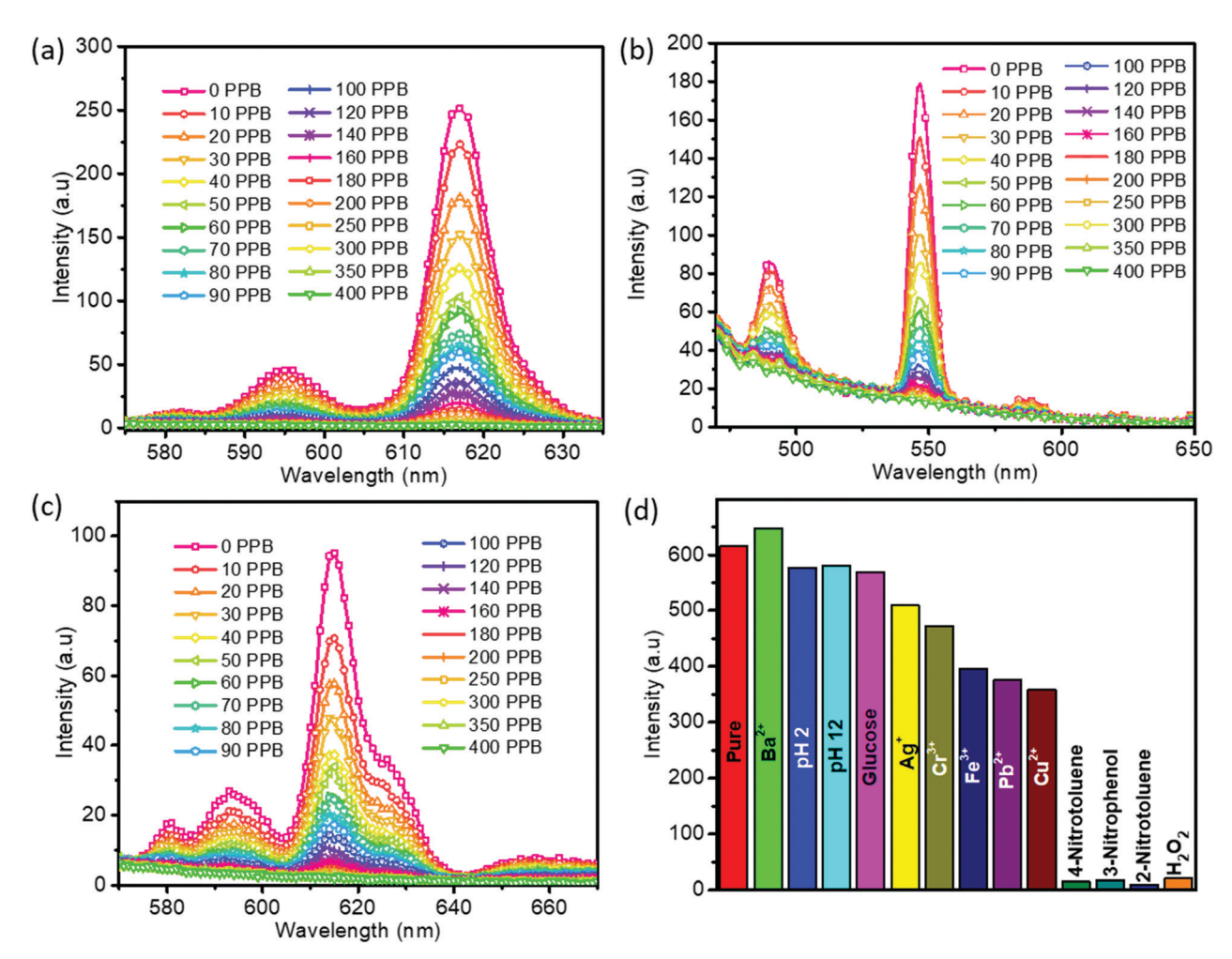


Fig. 8 PL response of (a)  $BaWO_4$ :5Tb-5Eu, (b)  $BaWO_4$ :5Tb, and (c)  $BaWO_4$ :5Eu nanofibers dispersed in water towards 2-nitrotoluene concentration, and (d) selectivity of  $BaWO_4$ :5Tb-5Eu nanofiber dispersion in water towards 2-nitrotoluene and  $H_2O_2$ .

The super adsorption of cationic dyes on BaWO<sub>4</sub> nanostructures is corroborated to the electrostatic interaction between the dye and the partial negative charges on the surface of BaWO<sub>4</sub>. 45 Apparently, BaWO<sub>4</sub> nanofibers can be a super adsorbent towards 2-nitrotoluene through the electrostatic bonding between the partial negative charges of the BaWO<sub>4</sub> surface and the partial positive  $(\delta^{+})$  charge of the benzene rings of 2-nitrotoluene (formed by the electron pulling of N<sup>+</sup> ions). This interaction is evident in the FTIR absorbance spectra (Fig. S7a and b, ESI†) of BaWO<sub>4</sub>:5Tb-5Eu nanofibers in the presence and absence of 2-nitrotoluene. The peak originating from the  $[WO_4]^{2-}$  ligand of BaWO4 is shifted to lower wavenumbers in the presence of 2-nitrotoluene, which can be ascribed to the hindrance in the vibration of the  $[WO_4]^{2-}$  ligand induced by 2-nitrotoluene, which is obvious from Fig. S7b (ESI†). The subsequent changes in the peak position of the benzene rings of 2-nitrotoluene are also observed vice versa in the FTIR spectrum of BaWO4 in the presence of 2-nitrotoluene.

Additionally, on comparing the UV absorption spectra of the analytes and the emission spectra of the pure  $BaWO_4$ , as in Fig. S8 (ESI $\dagger$ ), the UV absorption of the nitroaromatic analytes overlaps with the emission spectra of the pure  $BaWO_4$  nanofibers. The UV

spectra of the nanofibers, shown in Fig. S9 (ESI†), do not reveal any significant absorption bands of RE3+ ions, though the PLE spectra (Fig. 5) reveal the weak absorbance of the RE<sup>3+</sup> ions overlapping the emission spectra of the BaWO<sub>4</sub> lattice. Apparently, one can conclude that there is a competition between the RE<sup>3+</sup> ions and the analytes to receive the energy non-radiatively from the excited lattice. Therefore, the anticipated donor-acceptor type energy transfer occurs between the lattice and the nitro-aromatic compounds than the RE<sup>3+</sup> ions in the presence of nitro-aromatics. The LUMO (lowest unoccupied molecular orbital) energy levels of 2,4,6-trinitrotoluene (TNT) and 2,4-dinitrotoluene (DNT) are smaller than that of 2-nitrotoluene; therefore, one can expect an easier electron transfer from the donor to TNT and DNT than to 2-nitrotoluene, hence an improved sensitivity towards TNT and DNT is expected. 9,46 A schematic of the energy-transfer quenching mechanism in the absence and presence of 2-nitrotoluene is presented in Fig. S10 (ESI†). A slightly higher quenching percentage for BaWO<sub>4</sub>:5Tb-5Eu as compared to BaWO<sub>4</sub>:5Tb and BaWO<sub>4</sub>:5Eu is observed at room temperature besides the high-intensity emission and relative quantum yield from the BaWO<sub>4</sub>:5Tb-5Eu nanofibers.

The Stern-Volmer plots of the relative luminescence intensity  $(I_0/I)$  *versus* the concentration of 2-nitrotoluene are shown

Journal of Materials Chemistry C

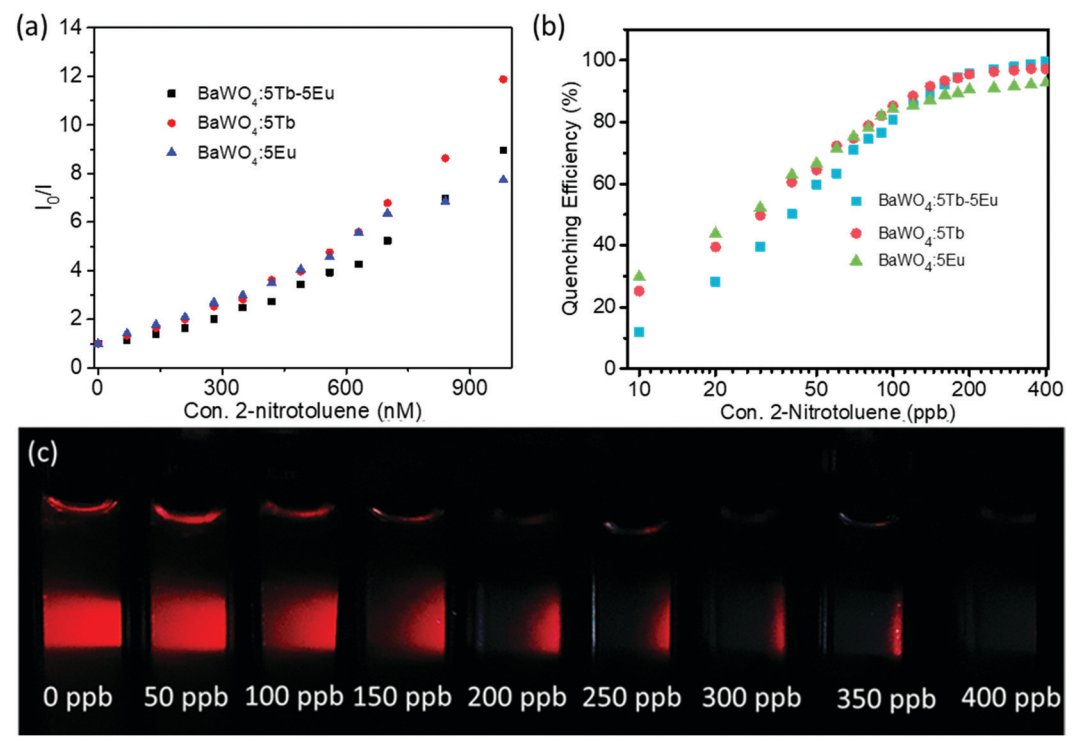


Fig. 9 (a) Stern–Volmer plots and (b) quenching efficiency of RE<sup>3+</sup> doped BaWO<sub>4</sub> nanofibers and (c) extinction of luminescence with increasing concentration of 2-nitrotoluene for nanofibers dispersed in water.

in Fig. 9a. The Stern-Volmer plots of BaWO<sub>4</sub>:5Tb-5Eu, BaWO<sub>4</sub>:5Tb, and BaWO<sub>4</sub>:5Eu can be fitted well to the exponential equations 1.67e<sup>1.80×10<sup>6</sup>[NT]</sup> - 0.719, 3.88e<sup>1.33×10<sup>6</sup>[NT]</sup> - 3.15, and 2.45e<sup>1.62×10<sup>6</sup>[NT]</sup> - 1.36, respectively. The Stern-Volmer curves are nonlinear as compared to the typical linear ones which may be a result of simultaneous static and dynamic quenching.  $^{47}$ 

The quenching coefficients are calculated using the equation, 97

$$I_0/I = (K_D[NT] + 1)(K_S[NT] + 1)$$
 (1)

where  $I_0$  and I are the fluorescence intensity in the absence and presence of 2-nitrotoluene,  $K_{\rm D}$  is the dynamic quenching constant,  $K_{\rm S}$  is the static quenching constant and [NT] is the concentration of 2-nitrotoluene. The calculated quenching constants are  $K_{\rm D}=K_{\rm S}=1.73\times10^6$  and  $2.1\times10^6$ , and  $2.2\times10^6$  L mol<sup>-1</sup> for BaWO<sub>4</sub>:5Tb–5Eu, BaWO<sub>4</sub>:5Tb, and BaWO<sub>4</sub>:5Eu nanofibers, respectively, in the low-concentration range.

The dramatically high quenching constants reveal the very high sensitivity of the nanofibers towards the detection of explosive taggants. The detection limit (LOD) was calculated according to the equation: LOD =  $3S_0/K$ , where  $S_0$  is the standard deviation of blank RE<sup>3+</sup> doped BaWO<sub>4</sub> nanofiber emission (n=10), and K is the slope of the calibration graph.<sup>27</sup> The LOD is estimated in the range of 35–45 nM for the three different nanofibers. On comparing the literature data available for the detection of nitro-compounds using various luminescent materials, the performance of inorganic RE<sup>3+</sup> doped BaWO<sub>4</sub> nanofibers exceeds most of them, as listed in Table 3.

The quenching efficiency (QE =  $(I_0 - I)/I_0 \times 100$ ) curves of the nanofibers are shown in Fig. 9b. The increase in the concentration of 2-nitrotoluene enhances the quenching efficiency; however, a steady increase in efficiency is observed at lower concentrations of 2-nitrotoluene, which has a linear relationship with ln[NT]. The quenching phenomenon can also be observed by the naked eye under 247 nm UV excitation, as annihilation of the red luminescence with the stepwise addition of 2-nitrotoluene as in Fig. 9c. In the presence of 2-nitrotoluene, the luminescence intensity of the RE3+ doped BaWO4 nanofibers is drastically reduced and the response time is measured in the presence of 400 ppb 2-nitrotoluene, as shown in Fig. 10a. The results show that all the nanofibers exhibit a similar response time, which is less than one second. The photostability of the BaWO<sub>4</sub> nanofibers is measured under irradiation at 247 nm for 60 min (see Fig. 10b). For BaWO<sub>4</sub>:5Tb-5Eu and BaWO<sub>4</sub>:5Eu nanofibers, the intensity at 617 nm is monitored and for BaWO<sub>4</sub>:Tb nanofibers, the intensity at 545 nm emission is monitored to study the effect of photobleaching. Photobleaching is negligible in all the fibers. However, high stability is observed in the case of BaWO<sub>4</sub>:5Tb-5Eu nanofibers. The high stability of these nanowires under UV light can increase the lifespan of this material as a sensor.<sup>59</sup>

The fluorescence quenching characteristics using BaWO<sub>4</sub>: 5Tb-5Eu nanofibers as the representative nanofibers towards  $\rm H_2O_2$  are also studied, as shown in Fig. 11a. A gradual reduction in the luminescence intensity is observed in the presence of different concentrations of  $\rm H_2O_2$ . From the Stern-Volmer plot, Fig. 11b, the calculated quenching constants in the low-concentration range are  $K_{\rm D} = K_{\rm S} = 2.71 \times 10^4$  L mol<sup>-1</sup>.

Table 3 Comparison of RE<sup>3+</sup> doped BaWO<sub>4</sub> nanofibers with luminescent explosive probes reported in the literature

S. no.	Material	Quenching constant ( $L \text{ mol}^{-1}$ )	Limit of detection $(\mu M)$	Ref.
1	N-Doped graphene quantum dots	_	0.92	48
2	Cd(II) MOF	$7.4  imes 10^4$	_	12b
3	Dansyl conjugated tripodal AIEEgen	$3.79 \times 10^{7}$	0.001	49
4	Cd based MOFs	$6.56  imes 10^4$	2	50
5	Lysozyme capped CdS quantum dots	$3.28  imes 10^4$	0.1	51
6	Cu based MOFs	$1.6  imes 10^4$	3.2	26
7	Zr(IV) MOFS	$2.9  imes 10^4$	_	52
8	<i>p</i> -Phenylenevinylene	$8.53 \times 10^{4}$	0.035	53
9	Zn(II) MOFs	$1.09\times 10^4$	_	12 <i>a</i>
10	Zn(II) MOFs	$4.86 \times 10^{3}$	_	54
11	BaWO <sub>4</sub> :5Eu-5Tb nanofibers	$1.73 \times 10^{6}$	0.035	Present work
12	CdSe quantum dots	$1.31\times10^{5}$	0.021	27
13	Carbon dots	$5.99  imes 10^4$	0.2	55
14	Carbon quantum dots functionalized with amines	$2.31  imes 10^4$	2.57	56
15	Indium based MOFs	$1.65 \times 10^{5}$	0.32	57
16	Cd based MOFs	$5.42\times10^4$	8	58

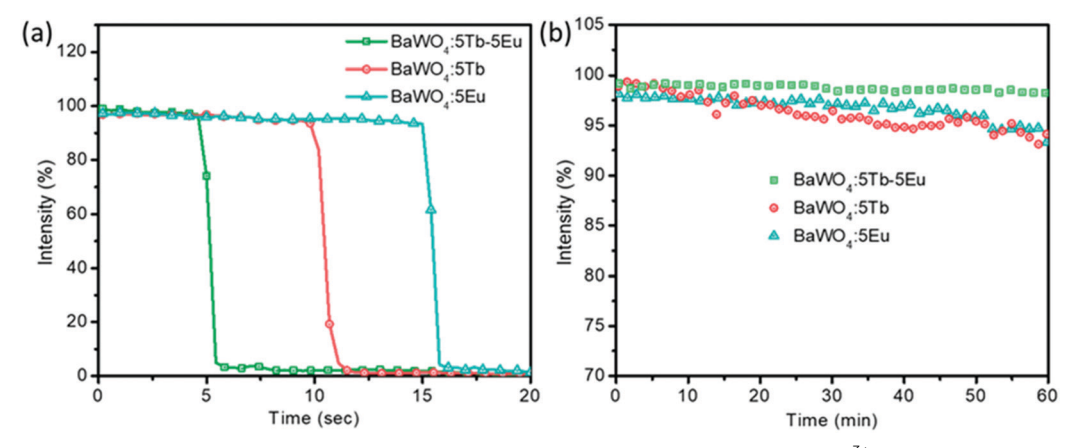


Fig. 10 (a) The response time for PL quenching in the presence of 2-nitrotoluene and (b) photobleaching of  $RE^{3+}$  doped  $BaWO_4$  nanofiber dispersions in water.

The response time observed here (Fig. 11c) is less than one second, which is rapid as compared to many other sensors reported in the literature. The LOD of BaWO<sub>4</sub>:5Tb–5Eu nanofibers towards  $\rm H_2O_2$  is 4  $\mu M$ . The Stern–Volmer constants and the LOD of the BaWO<sub>4</sub>:5Tb–5Eu nanofibers are on a par with the performance of the scheelite structured EuVO<sub>4</sub> nanoparticles

with the corresponding values of  $10^5$  L mol $^{-1}$  and 1.5  $\mu M$ , respectively,  $^6$  and the nanoparticle surface modified with luminescent molecules.  $^{60}$  The performance of the BaWO $_4$  nanofibers towards the sensing of  $H_2O_2$  is superior to BaGeF $_6$  and BaSiF $_6$  nanowires reported in our previous study.  $^{61}$  Importantly, the nanofibers are more practical in such studies as the recovery of

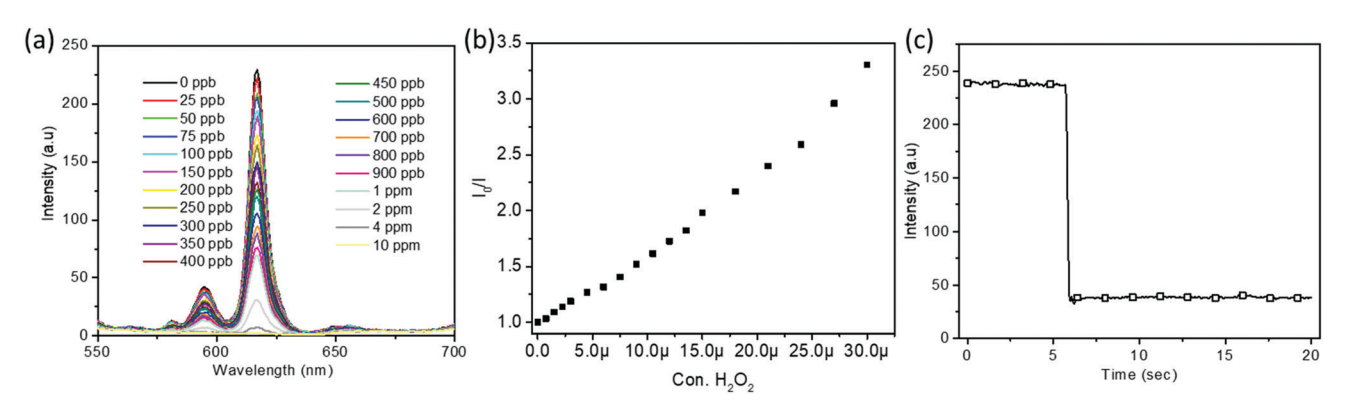


Fig. 11 (a) PL response of BaWO<sub>4</sub>:5Tb-5Eu nanofiber dispersion in water towards  $H_2O_2$  concentration, (b) Stern-Volmer plots, and (c) the response time for PL quenching in the presence of  $H_2O_2$ .

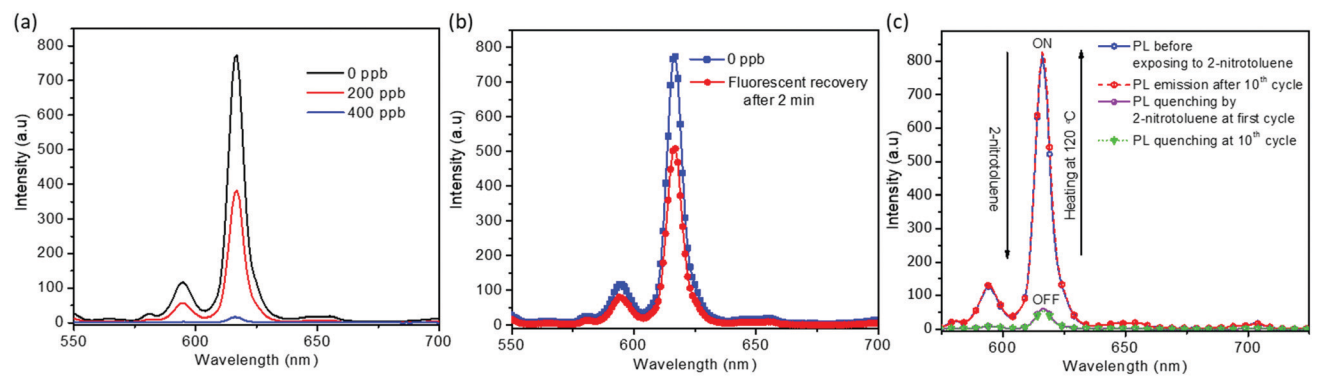


Fig. 12 (a) PL response of  $BaWO_4$ :5Tb-5Eu nanofibers in the solid state to 2-nitrotoluene, (b) sensor recovery under atmospheric conditions, and (c) sensor response during the repeated cycles.

the nanofibers is more convenient than the nanoparticles for repeated use.

The sensitivity of the BaWO<sub>4</sub>:5Tb-5Eu nanofibers in the solid state to the explosive vapors is also studied after pasting the nanofibers on a glass slide. The emission from the nanofibers pasted on the glass slide is recorded before and after exposing the nanofibers to a known quantity of 2-nitrotoluene vapors created by heating in a Petri dish as shown in Fig. S11 (ESI†). The characteristic emission from the nanofibers dropped drastically after exposing the nanofibers to the explosive vapors, akin to that in the solution, which is shown in Fig. 12a. The reversibility of the nanofibers as explosive sensors is achieved using 2-nitrotoluene as the model analyte. More than 60% of the luminescence emission is recovered after 2 min under normal atmospheric conditions after exposing the nanofibers to 400 ppb 2-nitrotoluene, as shown in Fig. 12b. However, the luminescence of the nanofibers is retained completely after heating at 120 °C for 10 min. The process is repeated up to 10 cycles, and the sensory response is retained as fresh nanofibers (Fig. 12c), revealing the high reversibility of these nanofibers, unlike many other disposable organic luminescent sensors. The stability of PL emission from the nanofibers in the solid state under prolonged UV excitation is assessed, which is shown in Fig. S12 (ESI†). The emission from the solid nanofibers is stable under UV light up to 60 minutes. Therefore, RE<sup>3+</sup> doped BaWO<sub>4</sub> nanofibers can be used as a simple, stable, reusable, versatile, and efficient sensor for the simultaneous detection of peroxide and nitro-organic explosives.

### Conclusions

High-aspect-ratio pure and rare-earth-doped BaWO<sub>4</sub> nanofibers were successfully fabricated through a sol–gel assisted electrospinning method. The nanofibers exhibited visible photoluminescence and cathodoluminescence emissions when codoped with varying mol% of Tb<sup>3+</sup>, and Eu<sup>3+</sup> rare-earth ions. The XRD analysis revealed the crystalline nature of the nanofibers with a tetragonal structure, and the structure is not affected by the rare-earth dopants. The PL emission monitored when excited by a 247 nm source can be tailored by adjusting the amount of Tb<sup>3+</sup> and Eu<sup>3+</sup> ions. The intense blue CL emission from pure BaWO<sub>4</sub>

nanofibers and green and red emissions from  $Tb^{3+}$  and  $Eu^{3+}$  doped nanofibers are observed, which is characteristic of these ions. The visible PL emissions from the  $RE^{3+}$  doped  $BaWO_4$  nanofibers are highly sensitive to 2-nitrotoluene and  $H_2O_2$  with quenching coefficients in the order of  $10^6$  and  $10^4$  L  $mol^{-1}$ , respectively, to 2-nitrotoluene and  $H_2O_2$ . The limits of detection of the nanofibers towards 2-nitrotoluene and  $H_2O_2$  are  $0.035-0.045~\mu M$  and  $1~\mu M$ , respectively. The performance of the  $RE^{3+}$  doped  $BaWO_4$  nanofibers is better than those of most of the organic materials reported for the detection of nitro-explosives and on a par with the scheelite structured  $EuVO_4$  nanoparticles for  $H_2O_2$  sensing. Rapid response, stability, and reusability identify this nanofiber material as a promising commercial sensor for highly selective and sensitive detection of explosives of two different origins.

## Conflicts of interest

There are no conflicts to declare.

## Acknowledgements

The authors would like to thank the Army Research Office (ARO), Department of Defense (DoD), for research funding, Contract No. W911NF1810469. The instrumentation was supported by the U.S. DoD grants W911NF-14-1-0060, W911NF-15-1-0566 and W911NF-09-1-0011, and the NSF MRI Program DMR 1626376. Use of the Center for Nanoscale Materials, an Office of Science user facility, was supported by the U.S. Department of Energy, Office of Science, Office of Basic Energy Sciences, under Contract No. DE-AC02-06CH11357.

## References

(a) X. Zhao and J. Yinon, J. Chromatogr. A, 2002, 946, 125–132;
 (b) M. Berg, J. Bolotin and T. B. Hofstetter, Anal. Chem., 2007, 79, 2386–2393;
 (c) S. Babaee and A. Beiraghi, Anal. Chim. Acta, 2010, 662, 9–13;
 (d) M. Najarro, M. E. D. Morris, M. E. Staymates, R. Fletcher and G. Gillen, Analyst, 2012, 137, 2614–2622;
 (e) P. Sulzer, F. Petersson, B. Agarwal, K. H. Becker, S. Jürschik,

- T. D. Märk, D. Perry, P. Watts and C. A. Mayhew, *Anal. Chem.*, 2012, **84**, 4161–4166; (f) S. Guo, D. Wen, Y. Zhai, S. Dong and E. Wang, *ACS Nano*, 2010, **4**, 3959–3968; (g) M. Y. Ho, N. D'Souza and P. Migliorato, *Anal. Chem.*, 2012, **84**, 4245–4247; (h) H.-X. Zhang, A.-M. Cao, J.-S. Hu, L.-J. Wan and S.-T. Lee, *Anal. Chem.*, 2006, **78**, 1967–1971; (i) M. Riskin, R. Tel-Vered and I. Willner, *Adv. Mater.*, 2010, **22**, 1387–1391; (j) S. S. R. Dasary, A. K. Singh, D. Senapati, H. Yu and P. C. Ray, *J. Am. Chem. Soc.*, 2009, **131**, 13806–13812; (k) Y. Ma, H. Li, S. Peng and L. Wang, *Anal. Chem.*, 2012, **84**, 8415–8421.
- (a) M. E. Germain and M. J. Knapp, *Chem. Soc. Rev.*, 2009, 38, 2543–2555; (b) H. Sohn, M. J. Sailor, D. Magde and W. C. Trogler, *J. Am. Chem. Soc.*, 2003, 125, 3821–3830; (c) J. V. Goodpaster and V. L. McGuffin, *Anal. Chem.*, 2001, 73, 2004–2011; (d) X. Sun, Y. Wang and Y. Lei, *Chem. Soc. Rev.*, 2015, 44, 8019–8061; (e) R. C. Stringer, S. Gangopadhyay and S. A. Grant, *Anal. Chem.*, 2010, 82, 4015–4019; (f) B. Gole, A. K. Bar and P. S. Mukherjee, *Chem. Commun.*, 2011, 47, 12137–12139; (g) D. Li, J. Liu, R. T. K. Kwok, Z. Liang, B. Z. Tang and J. Yu, *Chem. Commun.*, 2012, 48, 7167–7169; (h) N. Venkatramaiah, S. Kumar and S. Patil, *Chem. Commun.*, 2012, 48, 5007–5009.
- (a) Y. Xia, L. Song and C. Zhu, Anal. Chem., 2011, 83, 1401–1407;
  (b) D. Haldar, D. Dinda and S. K. Saha, J. Mater. Chem. C, 2016, 4, 6321–6326;
  (c) K. Zhang, H. Zhou, Q. Mei, S. Wang, G. Guan, R. Liu, J. Zhang and Z. Zhang, J. Am. Chem. Soc., 2011, 133, 8424–8427;
  (d) W. J. Peveler, A. Roldan, N. Hollingsworth, M. J. Porter and I. P. Parkin, ACS Nano, 2016, 10, 1139–1146.
- 4 (a) D. Banerjee, Z. Hu and J. Li, *Dalton Trans.*, 2014, 43, 10668–10685; (b) Y. Cui, Y. Yue, G. Qian and B. Chen, *Chem. Rev.*, 2012, 112, 1126–1162.
- 5 L. Senesac and T. G. Thundat, *Mater. Today*, 2008, **11**, 28–36.
- 6 N. Duée, C. Ambard, F. Pereira, D. Portehault, B. Viana, K. Vallé, D. Autissier and C. Sanchez, *Chem. Mater.*, 2015, 27, 5198–5205.
- 7 (a) R. S. Aparna, J. S. Anjali Devi, R. R. Anjana, J. Nebu and S. George, Sens. Actuators, B, 2019, 291, 298–305; (b) Q. Wang, D. J. Liu, L. L. Cui, X.-L. Hu, X.-L. Wang and Z.-M. Su, New J. Chem., 2019, 43, 963–969; (c) H. Turhan, E. Tukenmez, B. Karagoz and N. Bicak, Talanta, 2018, 179, 107–114; (d) W. Wu, N. Shi, J. Zhang, X. Wu, T. Wang, L. Yang, R. Yang, C. Ou, W. Xue, X. Feng, L. Xie and W. Huang, J. Mater. Chem. A, 2018, 6, 18543–18550.
- 8 M. S. Meaney and V. L. McGuffin, *Anal. Chim. Acta*, 2008, **610**, 57–67.
- S. S. Nagarkar, B. Joarder, A. K. Chaudhari, S. Mukherjee and S. K. Ghosh, *Angew. Chem.*, *Int. Ed.*, 2013, 52, 2881–2885.
- 10 Y. Xu, B. Li, W. Li, J. Zhao, S. Sun and Y. Pang, Chem. Commun., 2013, 49, 4764–4766.
- A. Tournebize, P. Wong-Wah-Chung, S. Thérias, P.-O. Bussière,
  A. Rivaton, T. Caron, F. Serein-Spirau, J.-P. Lère-Porte,
  P. Montméat and J.-L. Gardette, *Polym. Degrad. Stab.*, 2012,
  97, 1355–1365.
- 12 (a) X.-X. Wu, H.-R. Fu, M.-L. Han, Z. Zhou and L.-F. Ma, Cryst. Growth Des., 2017, 17, 6041–6048; (b) L. Yang, X. Li, C. Qin, K.-Z. Shao and Z.-M. Su, CrystEngComm, 2016, 18, 4765–4771.

- 13 (a) Z. Hou, P. Yang, C. Li, L. Wang, H. Lian, Z. Quan and J. Lin, Chem. Mater., 2008, 20, 6686-6696; (b) H. Farsi, Z. Barzgari and S. Z. Askari, Res. Chem. Intermed., 2015, 41, 5463-5474; (c) A. Sahmi, K. Bensadok and M. Trari, J. Photochem. Photobiol., A, 2017, 349, 36-41; (d) M. Li, Q. Meng, S. Li, F. Li, Q. Zhu, B.-N. Kim and J.-G. Li, Ceram. Int., 2019, 45, 10746-10755; (e) Y. Zhang, R. Fan, Q. Zhang, Y. Chen, O. Sharifi, D. Leszczynska, R. Zhang and Q. Dai, Mater. Res. Bull., 2019, 110, 169-173.
- 14 D. Wang, K. Pan, Y. Qu, G. Wang, X. Yang and D. Wang, *ACS Appl. Nano Mater.*, 2018, **1**, 4762–4770.
- 15 (a) L. S. Cavalcante, J. C. Sczancoski, N. C. Batista, E. Longo, J. A. Varela and M. O. Orlandi, Adv. Powder Technol., 2013, 24, 344–353; (b) M. J. Kim, H. Park and H. J. Kim, J. Korean Phys. Soc., 2016, 69, 1130–1134; (c) M. Moszyński, M. Balcerzyk, W. Czarnacki, A. Nassalski, T. Szczęśniak, H. Kraus, V. B. Mikhailik and I. M. Solskii, Nucl. Instrum. Methods Phys. Res., Sect. A, 2005, 553, 578–591; (d) Z. Shan, Y. Wang, H. Ding and F. Huang, J. Mol. Catal. Chem., 2009, 302, 54–58; (e) D. Spassky, V. Mikhailin, M. Nazarov, M. N. Ahmad-Fauzi and A. Zhbanov, J. Lumin., 2012, 132, 2753–2762.
- 16 P. Černý and H. Jelínková, Opt. Lett., 2002, 27, 360-362.
- 17 Y. Wang, Y. Qu, K. Pan, G. Wang and Y. Li, *Chem. Commun.*, 2016, 52, 11124–11126.
- 18 (a) S. Cho, Appl. Surf. Sci., 2018, 432, 202-206; (b) H. Wu, J. Yang, X. Wang, S. Gan and L. Li, Solid State Sci., 2018, 79, 85-92; (c) S. Vidya, S. Solomon and J. K. Thomas, Adv. Condens. Matter Phys., 2013, 409620, DOI: 10.1155/2013/409620; (d) V. Caracciolo, F. Cappella, R. Cerulli, A. D. Marco, M. Laubenstein, S. S. Nagorny, O. E. Safonova and V. N. Shlegel, Nucl. Instrum. Methods Phys. Res., Sect. A, 2018, 901, 150-155; (e) L. D. S. Alencar, A. Mesquita, C. A. C. Feitosa, R. Balzer, L. F. D. Probst, D. C. Batalha, M. G. Rosmaninho, H. V. Fajardo and M. I. B. Bernardi, Ceram. Int., 2017, 43, 4462-4469; (f) A. Sahmi, S. Omeiri, K. Bensadok and M. Trari, Mater. Sci. Semicond. Process., 2019, 91, 108-114; (g) L. I. Ivleva, I. S. Voronina, P. A. Lykov, L. Yu. Berezovskaya and V. V. Osiko, J. Cryst. Growth, 2007, 304, 108-113.
- (a) F.-Q. Dong, Q.-S. Wu and Y.-P. Ding, J. Alloys Compd., 2009, 476, 571–574; (b) K. Kawashima, J.-H. Kim, I. Cheng, K. Yubuta, K. Shin, Y. Liu, J. Lin, G. Henkelman and C. B. Mullins, Cryst. Growth Des., 2018, 18, 5301–5310; (c) H. Shi, L. Qi, J. Ma and H. Cheng, Chem. Commun., 2002, 1704–1705; (d) H. Shi, L. Qi, J. Ma and H. Cheng, J. Am. Chem. Soc., 2003, 125, 3450–3451; (e) Z. Luo, H. Li, J. Xia, W. Zhu, J. Guo and B. Zhang, Mater. Lett., 2007, 61, 1845–1848; (f) X. Zhao, T. Li, Y. Xi, D. H. L. Ng and J. Yu, Cryst. Growth Des., 2006, 6, 2210–2213; (g) L. Zhang, J.-S. Dai, L. Lian and Y. Liu, Superlattices Microstruct., 2013, 54, 87–95.
- 20 G. George and Z. Luo, *Curr. Nanosci.*, 2019, **15**, DOI: 10.2174/1573413715666190112121113.
- 21 (a) X. Wang, Y.-G. Kim, C. Drew, B.-C. Ku, J. Kumar and L. A. Samuelson, *Nano Lett.*, 2004, **4**, 331–334; (b) J. Yao,

- P. Ji, B. Wang, H. Wang and S. Chen, Sens. Actuators, B, 2018, 254, 110-119; (c) X. Wang, Y. Wang, Y. Shan, M. Jiang, M. Gong, X. Jin, X. Wang and J. Cheng, Talanta, 2018, 187, 179-187.
- 22 (a) H. Liu, J. B. Edel, L. M. Bellan and H. G. Craighead, Small, 2006, 2, 495-499; (b) F. Gu, H. Yu, P. Wang, Z. Yang and L. Tong, ACS Nano, 2010, 4, 5332-5338.
- 23 H. J. Walls, J. L. Davis and D. S. Ensor, US Pat., US20100177518A1, 2010.
- 24 S. Pagliara, A. Camposeo, A. Polini, R. Cingolani and D. Pisignano, Lab Chip, 2009, 9, 2851-2856.
- 25 (a) F. Quochi, F. Cordella, A. Mura, G. Bongiovanni, F. Balzer and H.-G. Rubahn, J. Phys. Chem. B, 2005, 109, 21690-21693; (b) A. Camposeo, F. D. Benedetto, R. Stabile, A. A. R. Neves, R. Cingolani and D. Pisignano, Small, 2009, 5, 562-566; (c) A. Camposeo, L. Persano and D. Pisignano, Macromol. Mater. Eng., 2013, 298, 487-503.
- 26 M. Jurcic, W. J. Peveler, C. N. Savory, D.-K. Bučar, A. J. Kenyon, D. O. Scanlon and I. P. Parkin, ACS Appl. Mater. Interfaces, 2019, 11, 11618-11626.
- 27 K.-Y. Yi, Forensic Sci. Int., 2016, 259, 101-105.
- 28 C. Peniche, D. Zaldívar, M. Pazos, S. Páz, A. Bulay and J. S. Román, J. Appl. Polym. Sci., 1993, 50, 485-493.
- 29 R. Chandrasekar, L. Zhang, J. Y. Howe, N. E. Hedin, Y. Zhang and H. Fong, J. Mater. Sci., 2009, 44, 1198.
- 30 B. Mistry, Handbook of Spectroscopic Data: Chemistry -UV, IR, PMR, CNMR and Mass Spectroscopy, Oxford Book Company, Jaipur, India, 2009.
- 31 Y.-J. Song, M. Wang, X.-Y. Zhang, J.-Y. Wu and T. Zhang, Nanoscale Res. Lett., 2014, 9, 17.
- 32 F. M. Pontes, M. A. M. A. Maurera, A. G. Souza, E. Longo, E. R. Leite, R. Magnani, M. A. C. Machado, P. S. Pizani and J. A. Varela, J. Eur. Ceram. Soc., 2003, 23, 3001-3007.
- 33 A. Phuruangrat, T. Thongtem and S. Thongtem, Superlattices Microstruct., 2012, 52, 78-83.
- 34 C. Duan, Z. Zhang, S. Rösler, S. Rösler, A. Delsing, J. Zhao and H. T. Hintzen, Chem. Mater., 2011, 23, 1851-1861.
- 35 H. Yin, Y. Li, J. Bai, M. Ma and J. Liu, J. Mater., 2017, 3, 144-149.
- 36 Z. Xia and W. Wu, Dalton Trans., 2013, 42, 12989-12997.
- 37 W. Deng, F. Chun, W. Li, H. Su, B. Zhang, M. Xie, H. Zhang, X. Chu, L. Jin, C. Luo and W. Yang, Langmuir, 2018, 34, 8499-8507.
- 38 B. Xiao and M. Schmidt, *Inorg. Chem.*, 2017, **56**, 14948–14959.
- 39 P. Jena, S. K. Gupta, N. K. Verma, A. K. Singh and R. M. Kadam, New J. Chem., 2017, 41, 8947-8958.
- 40 X. Liu and J. Lin, J. Mater. Chem., 2007, 18, 221-228.
- 41 Z. Lou and M. Cocivera, Mater. Res. Bull., 2002, 37, 1573-1582.

- 42 G. Li, Z. Hou, C. Peng, W. Wang, Z. Cheng, C. Li, H. Lian and J. Lin, Adv. Funct. Mater., 2010, 20, 3446-3456.
- 43 Z. Gao, Y. Hu, W. Sun and J. W. Drelich, Langmuir, 2016, 32, 6282-6288.
- 44 N. Kupka and M. Rudolph, Int. J. Min. Sci. Technol., 2018, 28, 373-384.
- 45 W. Che, G. Li, X. Liu, K. Shao, D. Zhu, Z. Su and M. R. Bryce, Chem. Commun., 2018, 54, 1730-1733.
- 46 A. Singh, D. P. Dutta, J. Ramkumar, K. Bhattacharya, A. K. Tyagi and M. H. Fulekar, RSC Adv., 2013, 3, 22580-22590.
- 47 J. Liu, Y. Zhong, P. Lu, Y. Hong, J. W. Y. Lam, M. Faisal, Y. Yu, K. S. Wong and B. Z. Tang, Polym. Chem., 2010, 1, 426.
- 48 M. Kaur, S. K. Mehta and S. K. Kansal, Spectrochim. Acta, Part A, 2017, 180, 37-43.
- 49 N. Tripathi, S. Sandhu, P. Singh, A. Mahajan, M. Kaur and S. Kumar, Sens. Actuators, B, 2016, 231, 79-87.
- 50 K.-M. Wang, L. Du, Y.-L. Ma and Q.-H. Zhao, Inorg. Chem. Commun., 2016, 68, 45-49.
- 51 W. Na, X. Liu, S. Pang and X. Su, RSC Adv., 2015, 5, 51428-51434.
- 52 S. S. Nagarkar, A. V. Desai and S. K. Ghosh, Chem. Commun., 2014, 50, 8915-8918.
- 53 N. Dey, S. K. Samanta and S. Bhattacharya, ACS Appl. Mater. Interfaces, 2013, 5, 8394-8400.
- 54 R.-X. Yao, X. Cui, X.-X. Jia, F.-Q. Zhang and X.-M. Zhang, Inorg. Chem., 2016, 55, 9270-9275.
- 55 A. B. Siddique, A. K. Pramanick, S. Chatterjee and M. Ray, Sci. Rep., 2018, 8, 1-10.
- 56 B. B. Campos, R. Contreras-Cáceres, T. J. Bandosz, J. Jiménez-Jiménez, E. Rodríguez-Castellón, J. C. G. Esteves da Silva and M. Algarra, Carbon, 2016, 106, 171-178.
- 57 A. Sharma, D. Kim, J.-H. Park, S. Rakshit, J. Seong, G. H. Jeong, O.-H. Kwon and M. S. Lah, Chem. Commun., 2019, 2, 1-8.
- 58 J. Wang, J. Wu, L. Lu, H. Xu, M. Trivedi, A. Kumar, J. Liu and M. Zheng, Front. Chem., 2019, 7, 244.
- 59 C. Ambard, N. Duée, F. Pereira, D. Portehault, C. Méthivier, C.-M. Pradier and C. Sanchez, J. Sol-Gel Sci. Technol., 2016, 79, 381-388.
- 60 (a) H. Chen, A. Fang, L. He, Y. Zhang and S. Yao, Talanta, 2017, **164**, 580–587; (b) Y. Ling, N. Zhang, F. Qu, T. Wen, Z. F. Gao, N. B. Li and H. Q. Luo, Spectrochim. Acta, Part A, 2014, 118, 315-320.
- 61 (a) G. George, M. D. Simpson, B. R. Gautam, D. Fang, J. Peng, J. Wen, J. E. Davis, D. Ila and Z. Luo, RSC Adv., 2018, 8, 39296-39306; (b) G. George, S. L. Jackson, Z. R. Mobley, B. R. Gautam, D. Fang, J. Peng, D. Luo, J. Wen, J. E. Davis, D. Ila and Z. Luo, J. Mater. Chem. C, 2018, 6, 7285-7294.